Geophysical Research Letters

RESEARCH LETTER
10.1029/2021GL093118

Key Points:

- Collapsed calderas are recognized in eastern Arabia Terra
- Ancient Martian crust may have far more collapsed calderas than commonly recognized
- Plains style caldera complexes could be a source of huge volumes of volcaniclastic materials on Mars

Supporting Information:

Supporting Information may be found in the online version of this article.

Correspondence to:

J. R. Michalski,
jmichal@hku.hk

Citation:

Chu, Y. Y. Y., Michalski, J. R., Wright, S. P., & Webb, A. A. G. (2021). Caldera collapse and volcanic resurfacing in Arabia Terra provide hints of vast under-recognized early Martian volcanism. *Geophysical Research Letters*, *48*, e2021GL093118. https://doi.org/10.1029/2021GL093118

Received 24 FEB 2021
Accepted 9 JUL 2021

Caldera Collapse and Volcanic Resurfacing in Arabia Terra Provide Hints of Vast Under-Recognized Early Martian Volcanism

Yin Yau Yoyo Chu[1,2], Joseph R. Michalski[1,2], Shawn P. Wright[1,2], and A. Alexander G. Webb[1,2]

[1]Division of Earth and Planetary Science, University of Hong Kong, Hong Kong, China, [2]Laboratory for Space Research, University of Hong Kong, Hong Kong, China

Abstract Arabia Terra is an ancient, geologically complex region of Mars. It is not typically described as volcanic because it lacks prominent, easily recognizable shield volcanoes. However, Arabia Terra contains flood lavas and widespread layered materials that might represent airfall pyroclastics from unknown sources. Here we explore the geology of some complex topographic depressions in Arabia Terra previously hypothesized to represent collapse features termed "plains style caldera complexes," an enigmatic category of volcanic feature on Mars characterized by surface collapse rather than construction of topographic shields. Geomorphological observations and geologic mapping carried out here support a volcanic origin of these features, providing a possible source for volcaniclastic sediments. The identification of caldera complexes in Arabia Terra raises the questions of how they are linked to the geotectonic setting of the region and whether similar features might be much more abundant in the ancient Martian crust than is currently recognized.

Plain Language Summary The most recognizable volcanoes on Mars correspond to large topographic shields, similar to Hawaiian volcanoes. These are constructional features built by layer upon layer of lava, with a summit caldera. It is possible that Mars contains many other volcanoes that are less recognizable, however, because they consist only of the caldera complex without the topographic rise built by lava. These calderas could signify much more explosive volcanism or collapse due to migration of magma in the subsurface, or both. In this work, we describe more identifications of plains style caldera complexes, which are collapsed calderas without the easily recognizable shield topography. We describe the geology of these calderas in the Arabia Terra region, their possible links to tectonic setting there, and the possibility that similar features are much more common on Mars than is currently understood.

1. Introduction

Many fundamental aspects of Martian geology are represented in Arabia Terra, one of the most ancient and geologically complex parts of the Martian surface (Irwin et al., 2013). Crater counts suggest that the crust in this region is extremely ancient (Tanaka, 1986), and geophysical data show that the crust is thinner than any other part of the southern highlands (Zuber, 2000). The region is speculated to contain evidence for an early, failed episode of plate tectonics (Sleep, 1994) or other forms of large scale structural-tectonic deformation (McGill, 2000). Arabia Terra contains a vast, thick and complex sedimentary record (Malin & Edgett, 2000), which might have formed entirely through dust deposition (Fergason & Christensen, 2008) from the Noachian (Tanaka, 2000) through to recent times (Annex & Lewis, 2020; Lewis et al., 2008). The region also contains ancient, deep, steep-sided depressions that likely represent Noachian or Early Hesperian calderas (Michalski & Bleacher, 2013). Modeling of the patterns of ash plumes and deposition suggests these putative calderas could be the source localities for thick ash deposits representing some of the layered materials (Kerber et al., 2013). Though Arabia Terra has experienced significant volcanic resurfacing (Tanaka et al., 2014), the idea that Mars as a whole contains a large number of collapse calderas not associated with shield topography remains controversial. Evaluating potential connectivity among caldera collapse, magmatism, crustal structure, tectonic setting and airfall sedimentation is critical to understanding the geology of Arabia Terra, and early Mars in general.

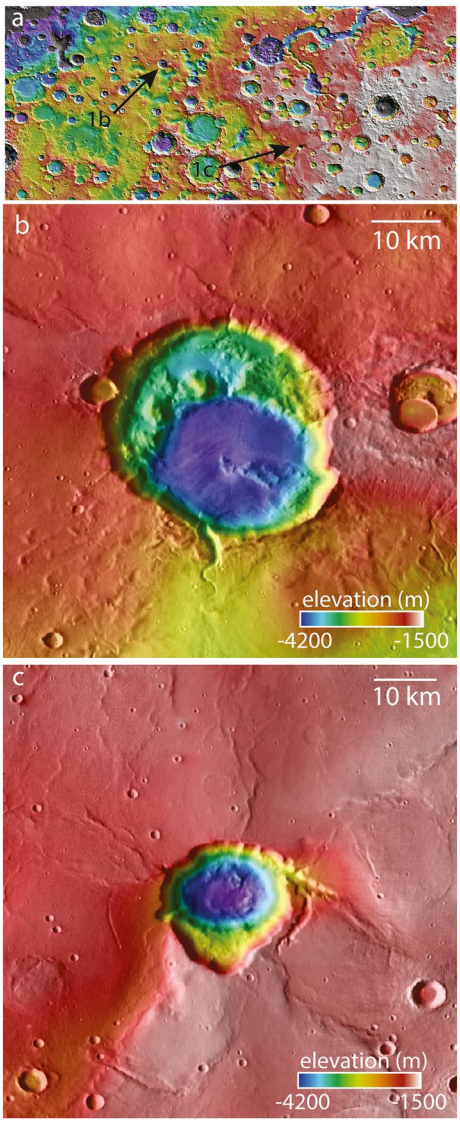

Figure 1. (a) Mars Orbiter Laster Altimeter (MOLA) elevation data are draped onto MOLA hillshade data showing the ancient, cratered surface of Arabia Terra. MOLA/HRSC merged elevation data draped onto Thermal Emission Imaging System daytime infrared data show (b) Siloe Patera and (c) Hiddekel Cavus, two deep, steep collapse features in northeastern Arabia Terra.

This work focuses on possible caldera structures in Arabia Terra. One potential "plains style caldera complex" described here is Siloe Patera, a set of nested depressions located at 35.3°N, 6.55°E, ~350 km south of the dichotomy boundary (Figure 1) (Michalski & Bleacher, 2013). With a ~40 km diameter and ~1.8 km depth, the depression has a depth/diameter ratio uncommon for any impact crater and extremely high for any ancient basin, which should become wider and shallower due to mass wasting over geologic time (Malin & Dzurisin, 1977). Models of the Martian lithospheric magnetic field suggest an anomaly at Siloe Patera, supporting the interpretation of a magma chamber at depth that formed after the magnetic dynamo shut off (Morschhauser et al., 2014). Another unusual feature, Hiddekel Cavus, a 20 km-wide, 2 km-deep depression located at 29.4°N, 16.2°E has an extremely high depth/diameter ratio and clear association with wrinkle ridges, arcuate faults and other indicators of collapse. In this paper, we describe the results of geomorphic and geologic mapping of these candidate caldera features, detailed observations of specific geologic relationships, and relationship of their features to established models for caldera formation.

2. Methods

Topography was analyzed using Mars Global Surveyor (MGS) Mars Orbiter Laster Altimeter (MOLA) data merged with elevation derived from the Mars Express (Mex) High Resolution Stereo Camera (HRSC) (Fergason et al., 2018). This is a unique data set available within JMARS amounting to a global Digital Elevation Model (DEM) informed by both MOLA and HRSC, at 200 m/pixel resolution. Topographic studies and 3D visualizing were performed via ArcScene using HRSC/MOLA elevation data and visible stereo images from the Mars Reconnaissance Orbiter Context Camera (CTX) and High Resolution Imaging Science Experiment (HiRISE).

Geomorphology was evaluated using visible and thermal infrared images. Thermal infrared data from the MO Thermal Emission Imaging System (THEMIS) available in a global 100 m/pixel mosaic within JMARS provide a mesoscale base map (Edwards et al., 2011). Visible images used here include high resolution data available from HRSC at 10–20 m/pixel, CTX at ~6 m/pixel and HiRISE at ~0.25 m/pixel. Data were obtained in radiometrically corrected and geometrically projected format and ingested into a geographic information system (GIS) for analysis and interpretation. Visible images were draped over digital topography in order to create 3D views of bedding and surface morphology.

Thermophysical properties were evaluated using THEMIS and MGS Thermal Emission Spectrometer (TES) data (Fergason et al., 2006; Golombek et al., 2005). The TES data were previously processed into a global thermal inertia data set, though at relatively coarse spatial resolution (8 pixels per degree). Despite the coarse spatial resolution, these data provide a stable and reliable measure of thermal inertia (J m^{-2} K^{-1} $s^{-1/2}$). Areas with high THEMIS TI translate to surfaces with coarser grains, rocky materials, better indurated materials or some combination of all three of these scenarios.

Geological mapping was carried out in ArcMap using CTX data as a base. Units were identified based on their surface textures, response to erosion, tone, bedding and stratigraphic and contact relationships. Due to the pervasive dust cover, compositional information was not used to help distinguish and interpret map units. Thermal inertia data however informed the geologic unit descriptions, despite the dusty nature of the surfaces.

3. Results

3.1. Siloe Patera

Siloe Patera comprises two overlapping topographic depressions. The larger outer basin has a depth of ~1–1.15 km and a size of 33 × 40 km. Nested within it, is a smaller 30 × 26 km "inner basin" with depth of ~0.8 km below the floor of the outer basin. The combined features have an approximate diameter of ~40 km and a depth of ~1.9 km, amounting to a depth/diameter ratio of ~0.048.

Siloe Patera has no raised rim and no observable ejecta blanket. These two aspects of impact geology could be removed or obfuscated by erosion, but the erosion required to remove the ejecta and subdue the raised rim would also generate sediment fill in the basin. The depth/diameter ratios of ancient, eroded craters (~0.01) are systematically smaller than the depth/diameter ratios of fresh craters (~0.05) because of this basin filling process (Robbins & Hynek, 2012). It is unlikely if not impossible that Siloe Patera could have experienced enough erosion to remove its impact-related original features without decreasing the depth/diameter ratio (Michalski & Bleacher, 2013).

The high depth diameter ratio and nested set of basins can both be explained as a set of co-located or overlapping impact craters of which there are many examples in the ancient Martian crust (See Supporting Information S1). One relevant example occurs at 0.6°N, 348.5°E, where a smaller unnamed crater of 31 km diameter occurs within a larger unnamed crater of 52 km diameter. With a maximum depth of ~2.7 km, this combined structure has a depth/diameter ratio of ~0.053, with similar overall morphometrics to Siloe. In comparison to the nested unnamed craters, which likely have an impact origin, Siloe Patera has: (a) a flatter floor and (b) steeper walls that meet the floor at (c) sharper angles. The unnamed craters have (d) more circular shapes in map view, (e) a more concave profile overall, (f) irregular floor deposits that are (g) distributed more evenly throughout the basin floor and surrounding plains, and (h) a more distinct raised rim on both the outer and inner crater basins (see Supporting Information S1).

Siloe Patera exhibits a number of other geologic characteristics unlike those of impact craters. Figure 2a shows the irregular wall of Siloe, which has a left-stepping trace at near 90-degree angles, reminiscent of fracture or fault-controlled erosion. Blocky sediment at the base of the irregular cliffs likely represents mass wasting deposits from catastrophic failure of the wall. A 3-D view of the east wall of Siloe Patera shows faults present within the wall, consistent with subsidence of the crater floor (Figure 2b) typical of calderas on Earth. The upper bench of the Siloe floor (i.e., the outer basin floor) contains abundant hills and hummocks of friable materials that seemingly have been readily eroded into smooth materials without blocks filling the depressions between hummocks (Figure 2c). These materials, which are not widespread, appear to be locally derived and could represent volcanic deposits near the source.

The inner basin floor exhibits a west-northwest trending low mountain range unlike the central peak of an impact crater in several important ways. One, there is no single peak or peak-ring structure, but rather a linear suite of hills and mountains trending throughout the basin floor. Two, the ridge is separated and slightly offset near the center of the basin by a topographic gap of ~2 km (Figure 2d). At this topographic break in the ridgeline, a north-trending suite of *en echelon*, shallow, elongate pits occur (Figure 2e).

Siloe has one set of long flows emanating from the southwest portion of the rim toward the southwest, which might represent a Martian ignimbrite. These deposits have lobate patterns and occur in a somewhat narrow band ~20 km wide and ~55 km long, with an apparent thickness of 10s–100s of m (Figure 2f). The deposits stand out from surrounding plains deposits in part because they contain fairly well-developed channels, which might indicate the relative susceptibility to erosion of these materials (Figures 2f, 3a and 3b).

Geologic mapping summarized here describes important spatial and temporal relationships among geomorphic features critical to interpretation of the two sites (see Supporting Information S1 for detailed explanations of mapping and crater counting). At Siloe Patera, the oldest geologic map units are Npu (Noachian plains units) and NHpu, a relatively younger Noachian undifferentiated plains unit (Figure 4). Crater counts carried out on each unit result in estimated surface ages of 3.75 Ga for Npu and 3.8–3.7 Ga for NHpu (see Supporting Information S1). Both units are interpreted as a mixture of eroded and redistributed volcanic and impact-generated crustal materials that predate the formation of Siloe Patera. Both plains units

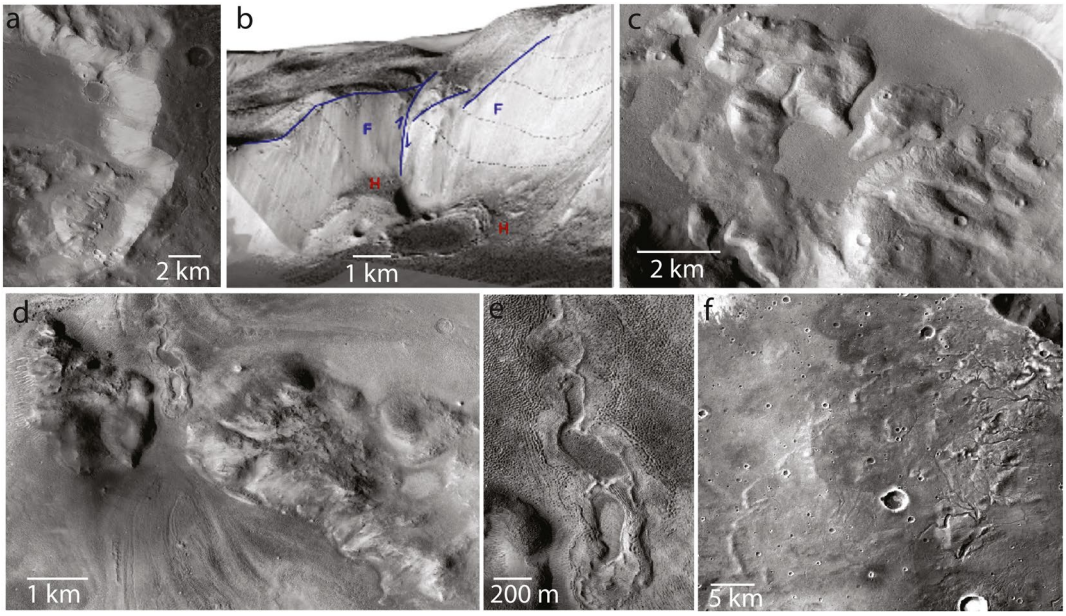

Figure 2. High resolution surface images illustrate key geological relationships at Siloe Patera. (a) The eastern wall has an irregular, stepped pattern unlike typical impact craters. (b) The irregular pattern is caused by fracturing and faulting, perspective view towards NNE with 3x vertical exaggeration, see Supporting Information S1) in the wall. (c) Floor materials contain hummocky, friable deposits, and (d) the lowermost floor contains hills rising ~150 m above the basin floor. (e) The WNW-trending mountain range is offset by a structural gap where a N-S trending series of *en echelon* pits occur. (f) Flow-like morphologies emanate toward the SW from the rim of Siloe Patera. The flows contain abundant channels.

are overlaid by Hfh, a Hesperian unit (3.3–3.5 Ga) exhibiting lobate topographic escarpments interpreted as flow fronts. Unit Hfh contains a high density of erosional channels, which might indicate a susceptibility of this unit to incision and erosion.

Within the basin of Siloe Patera are wall units (Hw) exposed in both the inner and outer basins, laterally bounded by faults in some areas, and various floor units. The floor of the outer basin contains a hummocky unit (Hho) dominated by irregular hills 10s–100s of meters high. Some of the topographically lower area between hills is filled with smooth material of similar albedo (Hso) interpreted as eroded, fine-grained material derived from the hummocks in Hho. The inner basin contains a blocky unit (Hbu) interpreted as mass

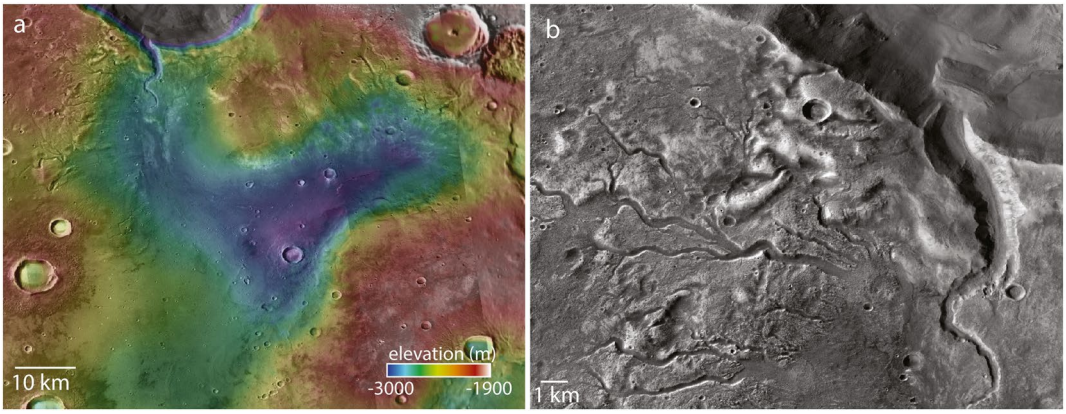

Figure 3. (a) HRSC/MOLA elevation data draped onto CTX images show that an irregularly shaped, ~600–700 m-deep depression occurs south of Siloe Patera. (b) The slopes of the perimeter of the depression contain networks of channels. The largest channel is ~3–4 km wide, 300–400 m deep, and ~15 km long. Where the channel empties into the southern rim of Siloe Patera, a wedge of sediment is immature and unlike any plausible delta morphology.

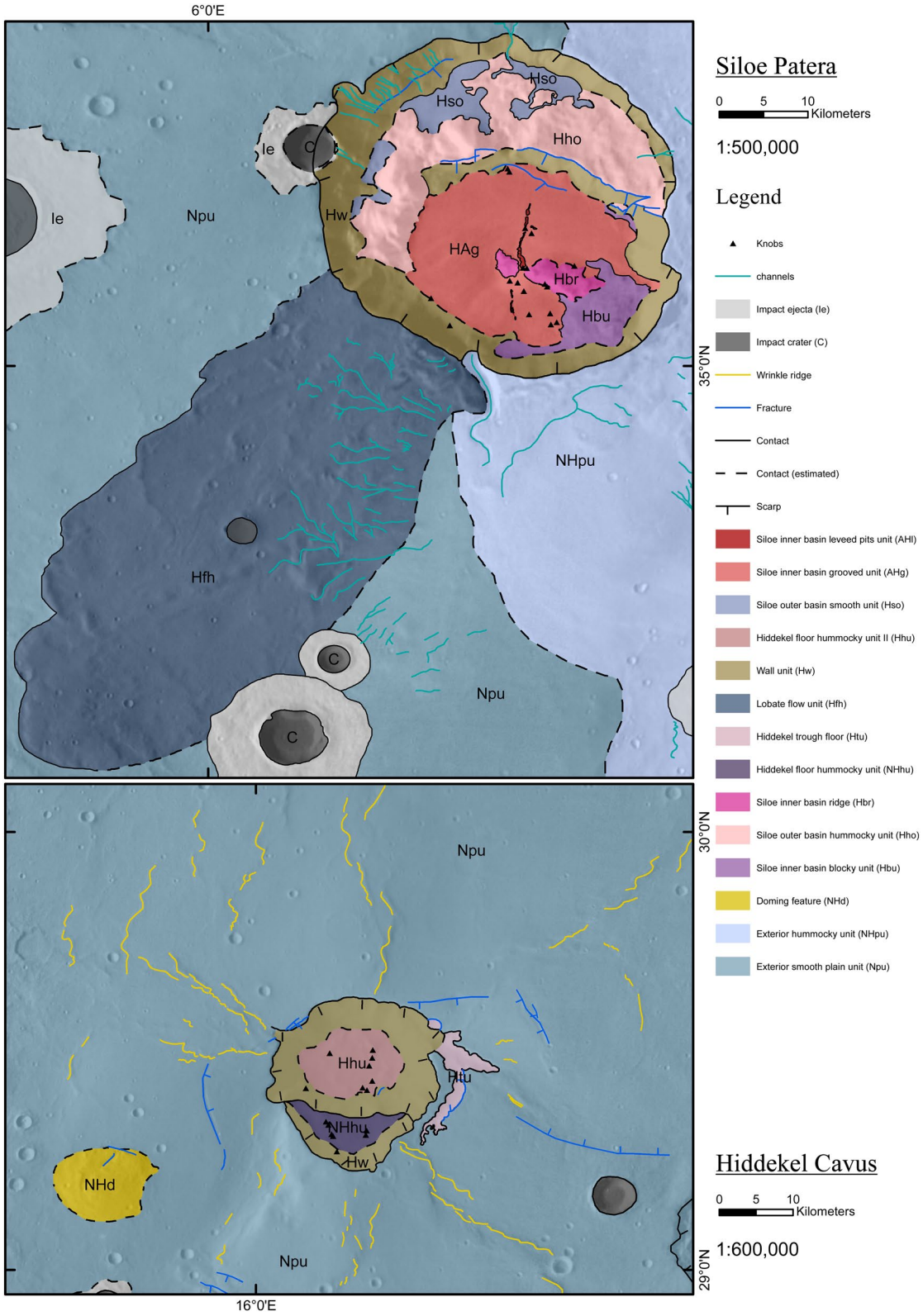

Figure 4. A geologic map of Hiddekel Cavus and Siloe Patera.

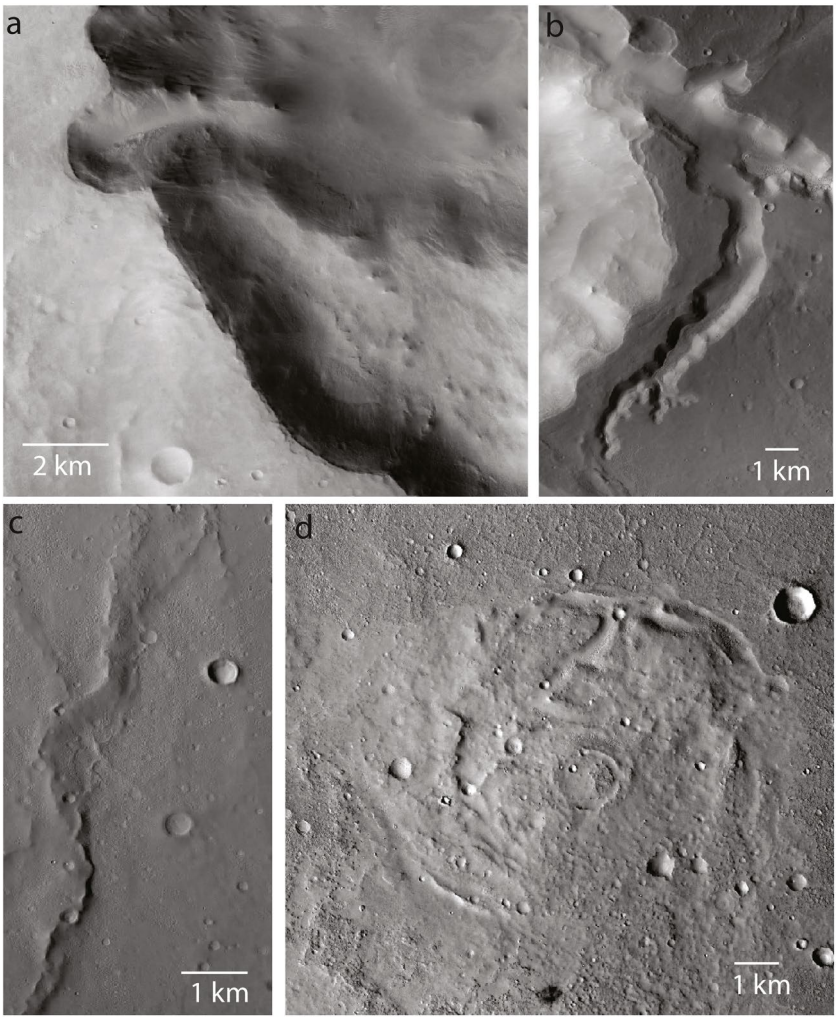

Figure 5. (a) Hiddekel Cavus contains a distinct tiered wall with a more gently sloping level ~10 km wide that is, ~1 km below the surface and ~1 km above the floor of the cavus. (b) An arcuate graben ~15 km long, 1–3 km wide and ~50–100 m deep occurs outside the eastern wall of the cavus. (c) Wrinkle ridges occur in a radial pattern emanating outward from the cavus. An unusual dome ~10 km wide rises ~100 m above the surface, west of the cavus.

wasting from the adjacent wall to the east, perhaps linked to structural dismemberment of the basin wall, and a prominent ridge unit (Hbr), which is composed of series of WNW-trending hills that rise 100s of m above the basin floor. The ~1-km-wide gap in the ridge exists where an apparent left-stepping offset in the ridge trend occurs. Orthogonal to that gap in the ridge is a NNE-trending suite of leveed pits meters-deep and 10s of meters diameter of unclear origins. The largest fraction of the inner basin is composed of a grooved floor unit (AHg) that lacks many impact craters and could be interpreted as ice-modified granular materials (e.g., a rock glacier or analogous material).

3.2. Hiddekel Cavus

Hiddekel Cavus is a deep topographic depression 20 km wide and 2.2 km deep. Like Siloe Patera, this feature lacks a raised rim, identifiable ejecta blanket, and any other indication of an impact origin. Also similar to Siloe Patera, Hiddekel Cavus is extremely deep and steep, with a depth/diameter ratio far outside of the values of impact craters impact crater (0.11). The depression is also composed of a tiered, bench structure where the southern wall contains a ~1 km-wide region of relatively shallowly sloping tiered surface located ~1 km elevation above the lowest basin floor and ~1 km below the exterior terrain (Figure 5a).

Hiddekel Cavus contains a prominent concentric graben structure ~15 km long, 1–3 km wide and 50–100 m deep located ~3–5 km outside the eastern rim of the cavus (Figure 5b). A striking feature of Hiddekel Cavus is that ~6 sets of wrinkle ridges 1–2 km wide and several 10s of km long occur in a radial pattern around the depression. Sets of fractures and fissures oriented perpendicular to the wrinkle ridges occur to the west and southwest (Figure 5c). A low topographic dome or shield ~10 km wide, rising ~100 m above the surrounding plains occurs in the adjacent plains ~20 km to the WSW of the cavus (Figure 5d). The size, height and morphology of the dome are similar to values for lunar domes and Icelandic shield volcanoes, suggesting this dome might have similar volcanic origins (Head & Gifford, 1980).

Hiddekel Cavus also occurs within an undifferentiated Noachian-Hesperian plains unit, though in the case of Hiddekel the plains have been deformed into a set of near-radial wrinkle ridges and an irregular set of escarpments and fractures. Like Siloe, the outer basin of Hiddekel has a hummocky floor unit (NHhu) and the inner basin contains a less-hummocky floor unit (Hhu), though grooves are not observed in Hiddekel. The inner basin floor units in both Hiddekel and Siloe are marked by small hummocks, unlike the large topographic undulations observed in the "hummocky" units. A concentric set of curvilinear fractures are observed to the east of the eastern basin wall, representing a 1–3 km-wide graben containing undifferentiated floor materials (unit Htu). Unit NHd includes the low topographic dome ~10 km wide and 10s of m elevation above the surrounding plains.

4. Discussion

Several lines of evidence point to a volcanic/magmatic origin for the collapse features at Siloe Patera and Hiddekel Cavus. First, the lobate flow features observed within the Hfh unit, indicate the possibility of a volcanic or pyroclastic flow deposit, fed by magmatic activities before or during the formation of the calderas. Second, arcuate fault scarps were observed within the wall unit (Hw) with higher thermal inertia and signs of mass wasting under the irregular cliffs, suggesting correlation with slip faulting during caldera collapse processes (Figure 2a). Third, there are segments of arcuate faults with length up to 9–11 km are located on the outer basin slope of and on the inner basin floor.

Another piece of evidence for a volcanic origin of Siloe is the relay ramp structure and breached relay ramp feature identified in this study that connects the two depressions, suggesting a fault-bounded relationship that indicates the nested depression was formed by catastrophic failure instead of impact cratering processes (Figure 2b). The linear feature on the inner basin floor might represent volcanic pits and craters. Unit AHI shows evidence of linear tensional fractures with interlinking leveed pits, here interpreted as the result possible fissure-controlled volcanism (Figure 2e).

Besides the lack of typical features of impact craters and signature showing excavation processes, the Siloe co-located depressions can be interpreted as nested calderas. The volcanic deposits, arcuate fault scarps and sets of normal faulting features observed within Siloe would thus have formed during two caldera collapse episodes.

South of Siloe Patera is a large, northeast trending valley ~80 km long, 20–40 km wide and ~700 m deep (Figure 3a) reminiscent of sagging associated with terrestrial calderas (Figure S6). Channels draining toward the basin floor occur along the perimeter of the basin. One large (3–4 km wide, 300–400 m deep, and ~15 km long), immature (i.e., low sinuosity) channel occurs where the depression intersects the southern rim of Siloe Patera (Figure 3b). But it bears noting that the location of this terminal channel is not in the deepest part of the basin, likely suggesting that the basin continued to subside after the formation of the channel. As with downsagging of calderas on Earth (Figure S6), the subsidence was likely caused by withdrawal of an adjacent magma chamber at depth or deep-seated structural discontinuities (Lipman, 1997).

Hiddekel Cavus shows typical caldera features including radiating wrinkle ridges as well as deflation and inflation signatures. There is no direct link between flows emanating from the cavus, as are observed in Siloe Patera. But the broad plains containing wrinkle ridges might be composed largely of volcanic materials. Further, the spatial association with dome/shield type constructional volcanic features may indicate evolution of volcanic processes in the Hiddekel area.

On Earth, explosive volcanism is generally associated with felsic magmatism, but there are examples of explosive basaltic volcanism such as the Masaya Caldera Complex in Nicaragua. Here, deeper than usual magma sources coupled with rapid ascent rates resulted in explosive basaltic volcanism (Gregg & Williams, 1996). A similar scenario could exist on Mars considering that the mafic crust is generally much thicker than on Earth. However environmental conditions and lower crustal pressures owing to lower gravity conditions on Mars could systematically result in more explosive volcanism on the red planet (Wilson & Head, 1994). Widespread layered sedimentary materials might actually represent pyroclastic deposits from collapse calderas underrecognized in the Martian geologic record.

5. Conclusions

Siloe Patera and Hiddekel Cavus likely both formed from surface collapse. At Siloe Patera, the association of the nested topographic depressions associated with faulting and subsidence of the basin floor, the occurrence of topographic sagging outside the basin, flow-like deposited emanating from the patera rim, and hummocks, spires and fissures in the basin floor all point to a likely volcanic origin. At Hiddekel, a similar history is reflected by the connective association of nested collapse, concentric faulting, radial wrinkle ridges as well as hummocks, spires and friable materials on the depression floor. Both features likely formed through surface collapse associated with magmatism. These plains style caldera complexes can only be identified through careful geomorphic observations, morphometrics and mapping, and thus they are likely much more common in the ancient crust of Mars than is currently recognized.

Data Availability Statement

The data used in this work were obtained by interfacing with JMARS, a free online geographic information system from Arizona State University (https://jmars.asu.edu/). THEMIS data can be found at http://viewer.mars.asu.edu/viewer/themis#T=0 and MOLA data are available at https://astrogeology.usgs.gov/search/map/Mars/GlobalSurveyor/MOLA/Mars_MGS_MOLA_DEM_mosaic_global_463m. HiRISE and CTX imaging data are available at https://pds-imaging.jpl.nasa.gov/volumes/mro.html. There are no other data sets used in this study.

Acknowledgments
This work was supported by the Research Grants Council, University Grants Committee (17301718).

References

Annex, A. M., & Lewis, K. W. (2020). Regional correlations in the layered deposits of Arabia Terra, Mars. *Journal of Geophysical Research: Planets*, *125*, e2019JE006188. https://doi.org/10.1029/2019JE006188

Edwards, C. S., Nowicki, K. J., Christensen, P. R., Hill, J., Gorelick, N., & Murray, K. (2011). Mosaicking of global planetary image datasets: 1. Techniques and data processing for Thermal Emission Imaging System (THEMIS) multi-spectral data. *Journal of Geophysical Research*, *116*, E10008. https://doi.org/10.1029/2010JE003755

Fergason, R. L., & Christensen, P. R. (2008). Formation and erosion of layered materials: Geologic and dust cycle history of eastern Arabia Terra, Mars. *Journal of Geophysical Research*, *113*(E12), E12001. https://doi.org/10.1029/2007je002973

Fergason, R. L., Christensen, P. R., & Kieffer, H. H. (2006). High-resolution thermal inertia derived from the Thermal Emission Imaging System (THEMIS): Thermal model and applications. *Journal of Geophysical Research*, *111*, E12004. https://doi.org/10.1029/2006JE002735

Fergason, R. L., Hare, T. M., & Laura, J. (2018). *HRSC and MOLA blended digital elevation model at 200m v2*.

Golombek, M. P., Arvidson, R. E., Bell, J. F., Christensen, P. R., Crisp, J. A., Crumpler, L. S., et al. (2005). Assessment of Mars Exploration Rover landing site predictions. *Nature*, *436*(7047), 44–48. https://doi.org/10.1038/Nature03600

Gregg, T. K. P., & Williams, S. N. (1996). Explosive mafic volcanoes on Mars and Earth: Deep magma sources and rapid rise rate. *Icarus*, *122*(2), 397–405. https://doi.org/10.1006/icar.1996.0132

Head, J. W., & Gifford, A. (1980). Lunar mare domes: Classification and modes of origin. *The Moon and the Planets*, *22*, 235–258. https://doi.org/10.1007/BF00898434

Irwin, R. P., Tanaka, K. L., & Robbins, S. J. (2013). Distribution of Early, Middle, and Late Noachian cratered surfaces in the Martian highlands: Implications for resurfacing events and processes. *Journal of Geophysical Research: Planets*, *118*(2), 278–291. https://doi.org/10.1002/jgre.20053

Kerber, L., Forget, F., Madeleine, J. B., Wordsworth, R., Head, J. W., & Wilson, L. (2013). The effect of atmospheric pressure on the dispersal of pyroclasts from martian volcanoes. *Icarus*, *223*(1), 149–156. https://doi.org/10.1016/J.Icarus.2012.11.037

Lewis, K. W., Aharonson, O., Grotzinger, J. P., Kirk, R. L., McEwen, A. S., & Suer, T. A. (2008). Quasi-periodic bedding in the sedimentary rock record of Mars. *Science*, *322*(5907), 1532–1535. https://doi.org/10.1126/Science.1161870

Lipman, P. W. (1997). Subsidence of ash-flow calderas: Relation to caldera size and magma-chamber geometry. *Bulletin of Volcanology*, *59*, 198–218. https://doi.org/10.1007/s004450050186

Malin, M., & Dzurisin, D. (1977). Landform degradation on Mercury, the Moon, and Mars: Evidence from crater depth/diameter relationships. *Journal of Geophysical Research*, *82*(2), 376–388. https://doi.org/10.1029/jb082i002p00376

Malin, M. C., & Edgett, K. S. (2000). Sedimentary rocks of early Mars. *Science*, *290*(5498), 1927–1937. https://doi.org/10.1126/science.290.5498.1927

McGill, G. E. (2000). Crustal history of north central Arabia Terra, Mars. *Journal of Geophysical Research*, *105*(E3), 6945–6959. https://doi.org/10.1029/1999je001175

Michalski, J. R., & Bleacher, J. E. (2013). Supervolcanoes within an ancient volcanic province in Arabia Terra, Mars. *Nature*, *502*(7469), 47–52. https://doi.org/10.1038/nature12482

Morschhauser, A., Lesur, V., & Grott, M. (2014). A spherical harmonic model of the lithospheric magnetic field of Mars. *Journal of Geophysical Research: Planets*, *119*, 1162–1188. https://doi.org/10.1002/2013JE004555

Robbins, S. J., & Hynek, B. M. (2012). A new global database of Mars impact craters ≥1 km: 1. Database creation, properties, and parameters. *Journal of Geophysical Research*, *117*(5), E05004. https://doi.org/10.1029/2011JE003966

Sleep, N. H. (1994). Martian plate tectonics. *Journal of Geophysical Research*, *99*(E3), 5639–5655. https://doi.org/10.1029/94JE00216

Tanaka, K. L. (1986). The stratigraphy of Mars. *Journal of Geophysical Research*, *91*(B13), E139–E158. https://doi.org/10.1029/JB091iB13p0E139

Tanaka, K. L. (2000). Dust and ice deposition in the Martian geologic record. *Icarus*, *144*(2), 254–266. https://doi.org/10.1006/icar.1999.6297

Tanaka, K. L., Skinner, J. A., Dohm, J. M., Irwin, R. P., Kolb, E. J., Fortezzo, C. M., et al. (2014). *Geologic map of Mars*. U.S. Geological Survey Geologic Investigations.

Wilson, L., & Head, J. W., III (1994). Mars: Review and analysis of volcanic eruption theory and relationships to observed landforms. *Reviews of Geophysics*, *32*(3), 221–263. https://doi.org/10.1029/94rg01113

Zuber, M. T. (2000). Internal structure and early thermal evolution of Mars from Mars global surveyor topography and gravity. *Science*, *287*, 1788–1793. https://doi.org/10.1126/science.287.5459.1788

References From the Supporting Information

Acocella, V. (2006). Caldera types: How end-members relate to evolutionary stages of collapse. *Geophysical Research Letters, 33*, L183148–L20320. https://doi.org/10.1029/2006gl028390.

Gudmundsson, A. (2008). Magma-chamber geometry, fluid transport, local stresses and rock behaviour during collapse caldera formation. In J. Gottsmann, & J. Martí (Eds.), *Caldera volcanism: Analysis, modelling and response* (pp. 313–349). Elsevier. https://doi.org/10.1016/s1871-644x(07)00008-3

Hartmann, W. K. (2005). Martian cratering 8: Isochron refinement and the chronology of Mars. *Icarus*, *174*(2), 294–320. https://doi.org/10.1016/j.icarus.2004.11.023

Ivanov, B. A. (2001). Mars/Moon cratering chronology and the evolution of Mars. *Space Science Reviews*, *96*.

Kneissl, T., van Gasselt, S., & Neukum, G. (2011). Map-projection-independent crater size-frequency determination in GIS environments — New software tool for ArcGIS. *Planetary and Space Science*, *59*, 1243–1254. https://doi.org/10.1016/j.pss.2010.03.015

Michael, G. G. (2013). Planetary surface dating from crater size–frequency distribution measurements: Multiple resurfacing episodes and differential isochron fitting. *Icarus*, *226*(1), 885–890. https://doi.org/10.1016/j.icarus.2013.07.004